JASA ARTICLE

Comparison of one-dimensional and three-dimensional glottal flow models in left-right asymmetric vocal fold conditions[a)]

Tsukasa Yoshinaga,[1,b)] Zhaoyan Zhang,[2] and Akiyoshi Iida[1]
[1]Department of Mechanical Engineering, Toyohashi University of Technology, 1-1 Hibarigaoka, Tenpaku, Toyohashi 441-8580, Japan
[2]Department of Head and Neck Surgery, University of California, Los Angeles, 31-24 Rehabilitation Center, 1000 Veteran Avenue, Los Angeles, California 90095-1794, USA

ABSTRACT:
While the glottal flow is often simplified as one-dimensional (1D) in computational models of phonation to reduce computational costs, the 1D flow model has not been validated in left-right asymmetric vocal fold conditions, as often occur in both normal and pathological voice production. In this study, we performed three-dimensional (3D) and 1D flow simulations coupled to a two-mass model of adult male vocal folds and compared voice production at different degrees of left-right stiffness asymmetry. The flow and acoustic fields in 3D were obtained by solving the compressible Navier-Stokes equations using the volume penalization method with the moving vocal fold wall as an immersed boundary. Despite differences in the predicted flow pressure on vocal fold surface between the 1D and 3D flow models, the results showed reasonable agreement in vocal fold vibration patterns and selected voice outcome measures between the 1D and 3D models for the range of left-right asymmetric conditions investigated. This indicates that vocal fold properties play a larger role than the glottal flow in determining the overall pattern of vocal fold vibration and the produced voice, and the 1D flow simplification is sufficient in modeling phonation, at least for the simplified glottal geometry of this study. © *2022 Acoustical Society of America*. https://doi.org/10.1121/10.0014949

(Received 12 August 2022; revised 4 October 2022; accepted 6 October 2022; published online 1 November 2022)
[Editor: Susanne Fuchs] Pages: 2557–2569

I. INTRODUCTION

Human voice is produced by interactions between the vocal folds and airflow within the glottis. This airflow is complex and exhibits three-dimensional (3D) phenomena including flow separation, vortex generation and shedding, jet flapping, and transition to turbulence (Neubauer *et al.*, 2007; Pickup and Thomson, 2009). Modeling and simulating these 3D airflow phenomena are challenging and computationally expensive. Therefore, the glottal airflow is often simplified as a one-dimensional (1D) flow that separates from the vocal fold surface somewhere within the glottis, and the pressure distribution on vocal fold surface upstream the flow separation point is calculated using Bernoulli's equation [e.g., Ishizaka and Flanagan (1972)]. The flow separation point can be either a fixed location on vocal fold surface or allowed to move along the vocal fold surface [e.g., Pelorson *et al.* (1994) and Kaburagi and Tanabe (2009)]. The 1D flow models have been widely used to investigate the physics of voice production (Ishizaka and Isshiki, 1976; Titze and Talkin, 1979; Steinecke and Herzel, 1995; Zhang, 2016a) and interpret experimental observations (Mergell *et al.*, 2000; Zhang and Luu 2012; Migimatsu and Tokuda, 2019). Due to their computational efficiency, 1D flow models are also widely used in articulatory synthesis systems [e.g., Maeda (1982), Story and Titze (1995), McGowan *et al.* (1995), Zañartu *et al.* (2007), Birkholz *et al.* (2015), Elie and Laprie (2016), and Zhang (2017)].

There have been many research efforts aiming to investigate to what extent the 1D flow model approximates the realistic glottal flow in modeling glottal fluid-structure interaction. de Vries *et al.* (2002) compared 1D flow model with a 2D incompressible Navier-Stokes flow model coupled to a two-mass model, and they found that the 1D model underestimated the phonation threshold pressure. Decker and Thomson (2007) compared 1D flow models with three separation prediction methods to a 2D Navier Stokes-based flow model, and their results showed that the mean intraglottal pressure and fundamental frequency were predicted by the 1D model, although the glottal flow was overpredicted by all 1D models. On the other hand, comparisons between the 1D flow model and physical model experiments demonstrated reasonable agreement in the phonation threshold pressure and fundamental frequency (Ruty *et al.*, 2007; Farahani and Zhang, 2016).

Despite these previous studies, it still remains unclear how accurate the 1D flow models are in modeling fluid-structure interaction in left-right asymmetric vocal fold conditions, as often occur in both normal phonation and pathological conditions. While there have been some studies investigating the glottal flow in left-right asymmetric vocal fold conditions using 2D or 3D flow models [e.g., Xue *et al.* (2010) and Falk *et al.* (2021)] or left-right asymmetric flow

[a)]Part of this study was presented at the 182nd Meeting of the Acoustical Society of America, Denver, CO, 24 May 2022 [J. Acoust. Soc. Am. **151**, A133 (2022)].
[b)]Electronic mail: yoshinaga@me.tut.ac.jp

patterns [e.g., Tao *et al.* (2007)], to the authors' knowledge, there have been no quantitative studies evaluating the capability of 1D flow-based models in accurately simulating the glottal fluid-structure interaction.

The goal of this study is to evaluate the accuracy of 1D flow-based models in simulating voice production in left-right asymmetric vocal fold conditions, by comparing voice production outputs predicted by simulations based on 1D and 3D flow models. To focus on the flow models and avoid the high computational costs associated with modeling 3D vocal folds, both the 1D and 3D flow models were coupled to a two-mass model of adult male vocal folds (Ishizaka and Flanagan, 1972). We conducted the 3D flow simulation by solving the compressible Navier Stokes equations coupled to the two-mass model in both left-right symmetric and asymmetric vocal fold conditions. Consideration of air compressibility in the 3D simulation allowed us to simulate the effect of subglottal pressure resonances as often observed in phonation experiments [e.g., Zhang *et al.* (2006)]. Vibratory characteristics and voice outcomes were then compared to those predicted by simulations using a 1D flow model. This comparison would allow us to evaluate how accurately the 1D flow model simulates voice production in left-right asymmetric vocal fold conditions.

II. METHODS

A. Two-mass vocal fold model and airway configuration

The two-mass model of the vocal folds consists of the upper and lower parts of the lumped masses (Ishizaka and Flanagan, 1972). The schematic of the two-mass model is depicted in Fig. 1. The masses are permitted only a medial-lateral motion and connected to the walls by a spring and a damper. In addition, the upper and lower masses are coupled by another spring. The equations of motion of each mass are written as

$$m_{1\alpha}\frac{d^2y_{1\alpha}}{dt^2}+r_1\frac{dy_{1\alpha}}{dt}+k_{1\alpha}y_{1\alpha}+k_{c\alpha}(y_{1\alpha}-y_{2\alpha})=F_{1\alpha}, \quad (1)$$

$$m_{2\alpha}\frac{d^2y_{2\alpha}}{dt^2}+r_2\frac{dy_{2\alpha}}{dt}+k_{2\alpha}y_{2\alpha}+k_{c\alpha}(y_{2\alpha}-y_{1\alpha})=F_{2\alpha}, \quad (2)$$

where m is the mass, y is the displacement, r is the damping coefficient, k is the spring constant, and F is the fluid force. The subscripts 1 and 2 indicate lower and upper mass, whereas the subscripts $\alpha = l$ and $\alpha = r$ indicate left and right side, respectively. Each mass had the shape of a cylinder with a diameter of $d_1 = 2.5$ mm and $d_2 = 0.5$ mm, and the cylinders are connected with a smooth wall which forms the tangential line for each cylinder as proposed by Pelorson *et al.* (1994). The glottal length l_g was set to 17 mm, typical of male vocal folds. When the left and right masses collide, the spring and damping constants of upper or lower mass are increased to model the additional collision forces. The time derivatives were discretized using the third-order Runge-Kutta method for both 3D and 1D flow models.

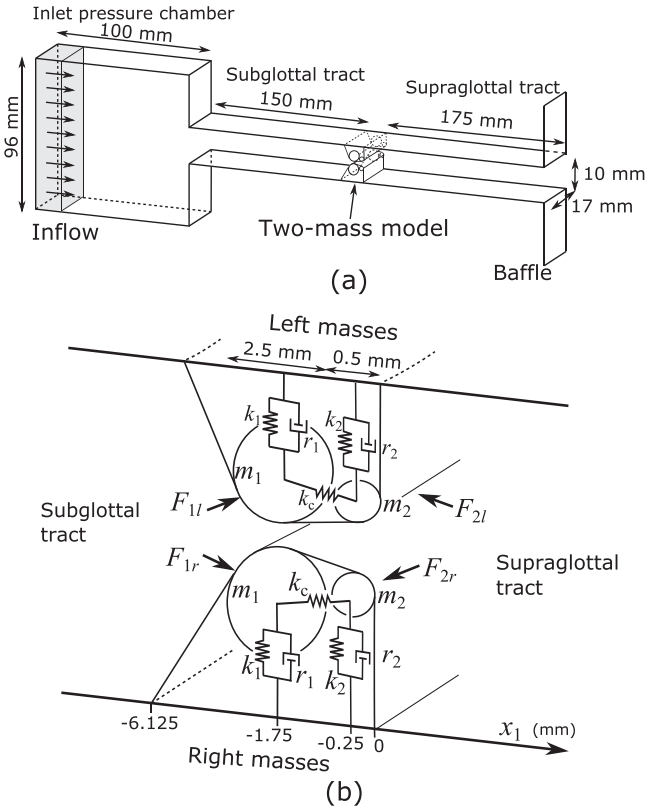

FIG. 1. Flow channel and two-mass model. (a) Flow channel from the inlet of pressure chamber to subglottal and supraglottal tracts. (b) Two-mass model with lumped-elements and tangential lines for left and right masses.

The flow channels upstream (subglottal) and downstream (supraglottal) of the vocal folds had a uniform cross-sectional area. For both channels, the width in the anterior-posterior direction was 17 mm, the same as the vocal fold length, while the medial-lateral dimension was set to 10 mm. The subglottal and supraglottal tract lengths were 150 and 175 mm, respectively. The upstream inlet chamber ($100 \times 96 \times 17$ mm) was set upstream of the supraglottal tract to represent the lungs. In this study, axes x_1, x_2, and x_3 were set to the superior-inferior, left-right (medial-lateral), and anterior-posterior directions, respectively. The origin of coordinate x_1 was set at the outlet of the upper masses or glottal exit as shown in Fig. 1.

To simulate the left-right tension imbalance, the spring constants and masses were multiplied by an imbalance parameter Q as

$$\begin{aligned} k_{1l} &= Qk_{1r}, \\ k_{2l} &= Qk_{2r}, \\ k_{cl} &= Qk_{cr}, \\ m_{1l} &= m_{1r}/Q, \\ m_{2l} &= m_{2r}/Q, \end{aligned} \quad (3)$$

in the same way as Ishizaka and Isshiki (1976). The imbalance parameter was varied from $Q = 1$ for the symmetric condition to 0.4, 0.6, 0.8, 1.2, 1.4, 1.6, and 3.0 for the asymmetric conditions. The parameters of spring constants,

https://doi.org/10.1121/10.0014949

damping coefficient, and mass values were chosen from Pelorson *et al.* (1994) as listed in Table I. The cross-sectional areas of glottal gaps A_{g1} and A_{g2} when the masses were at rest were set to 0. Hence, there was no glottal gap at the initial condition of the simulations.

B. 3D flow model

In the 3D flow model, the flow field was obtained by solving the compressible Navier Stokes equations. To consider the interaction between moving walls of the two-mass model and surrounding fluids, the volume penalization (VP) method (Liu and Vasilyev, 2007), one of the immersed boundary methods, was applied for the simulation. The governing equations are

$$\frac{\partial}{\partial t}\begin{pmatrix}\rho\\ \rho u_1\\ \rho u_2\\ \rho u_3\\ \rho E\end{pmatrix}+\frac{\partial}{\partial x_i}F_i=-(1/\phi-1)\chi\begin{pmatrix}\partial\rho u_i/\partial x_i\\ 0\\ 0\\ 0\\ 0\end{pmatrix}, \tag{4}$$

$$F_i=\begin{pmatrix}\rho u_i\\ \rho u_i u_1+p\delta_{i1}-\tau_{i1}\\ \rho u_i u_2+p\delta_{i2}-\tau_{i2}\\ \rho u_i u_3+p\delta_{i3}-\tau_{i3}\\ (\rho E+p)u_i-\tau_{ij}u_j-q_i\end{pmatrix}, \tag{5}$$

where ρ is the density, u_i are the flow velocities in x_i directions ($i=1, 2, 3$), E is the total energy, p is the pressure, δ_{ij} is the Kronecker delta, τ_{ij} is the viscous stress tensor, and q_i is the heat flux vector. The density and pressure are absolute values that satisfy the equation of state for ideal gas. The right-hand side of Eq. (4) is a penalization term of the VP method. The walls around the fluid are modeled as an external force associated with a porous medium with a porosity ϕ and using a mask function χ. The porosity was set to $\phi=0.25$ which results in a pressure reflectivity of 99%. The mask function is defined as

$$\chi=\begin{cases}\min(1,|d/\Delta x_2|) & \text{(inside object)}\\ 0 & \text{(fluid part)},\end{cases} \tag{6}$$

TABLE I. Spring constants, damping coefficient, and mass values for two-mass model.

Parameter	Symbol	Value	Value when collide
Lower spring constant	k_1	80 N/m	320 N/m
Upper spring constant	k_2	8 N/m	32 N/m
Coupling spring constant	k_c	55 N/m	
Lower damping constant	r_1	2.33×10^{-2} Ns/m	2.57×10^{-1} Ns/m
Upper damping constant	r_2	1.86×10^{-2} Ns/m	4.96×10^{-2} Ns/m
Lower mass	m_1	0.17 g	
Upper mass	m_2	0.03 g	

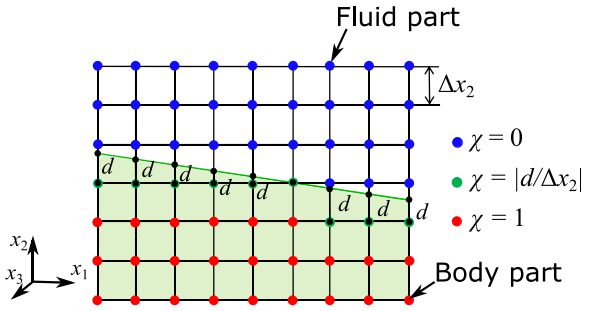

FIG. 2. (Color online) Fluid and body parts in the computational grid of the immersed boundary method. The mask function is calculated as proportional to the distance between the grid points and the actual wall position.

where d is the distance between the moving wall and the closest grid as shown in Fig. 2. By calculating the mask function proportion to the distance from the actual moving wall, the wall region smoothly moves through the grids.

The spatial derivatives of the governing equations were solved by a sixth-order compact finite-difference scheme, while the time integration was performed using the third-order Runge-Kutta method. To consider the turbulent flow around the vocal folds, the large eddy simulation was applied to filter the subgrid-scale turbulent energy using an implicit turbulence model with a 10th-order spatial filter. Details are described in Yoshinaga *et al.* (2020) and Yoshinaga *et al.* (2021).

The computational grids for the 3D flow simulation are shown in Fig. 3. For the finite-difference scheme, structured grids were constructed in the flow channel of the vocal folds and the outlet of the vocal tract. In the glottal flow channel, the minimum grid size was set to $\Delta x_1=0.05$ mm and $\Delta x_2=0.025$ mm. The grid sizes in x_1 and x_2 directions were

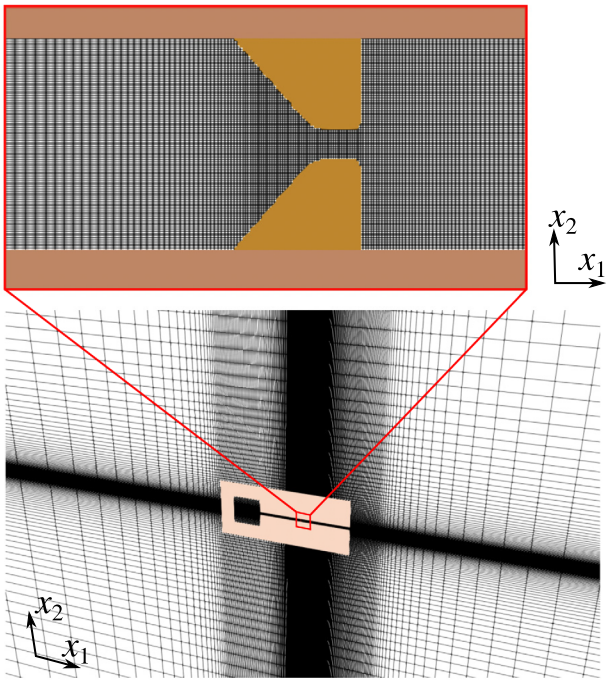

FIG. 3. (Color online) Computational grids for three-dimensional flow model.

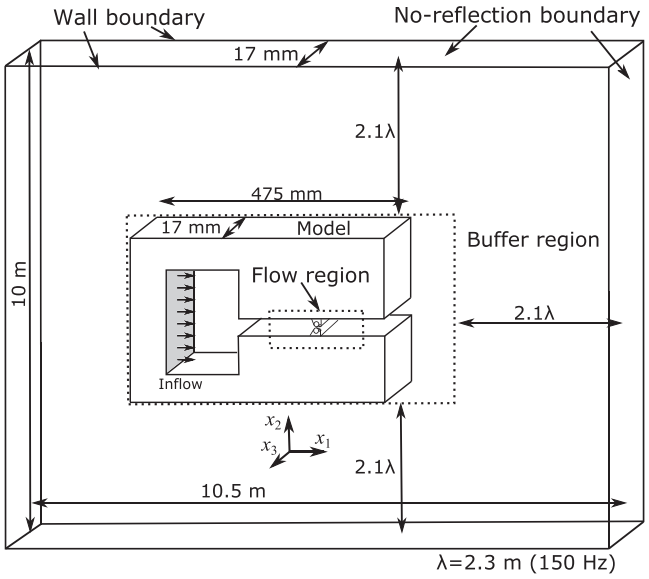

FIG. 4. Computational domain and boundary conditions.

gradually elongated towards the outlet of the flow channel to reduce the computational costs. The grid size of axis x_3 was kept to $\Delta x_3 = 0.1$ mm for the entire region. The accuracy of the current computational setup was validated by comparing to previously reported experimental data, as detailed in the Appendix.

The computational domain and boundary conditions are depicted in Fig. 4. A constant pressure of $p_{\text{in}} = 2$ kPa and a uniform velocity with a flow rate of 600 cm^3/s were set at the inlet of the chamber. Those values were chosen so that self-sustained oscillation was obtained in most of asymmetric vocal fold conditions investigated. At the outlet of the vocal tract, a buffer region, which eliminates the pressure and velocity fluctuations, was set to prevent any pressure reflections at the outlet of the computational domain. The non-reflection boundary condition was imposed in x_1 and x_2 directions at the outlet of the computational domain, while the non-slip wall was set on the outer boundary in x_3 direction for the entire domain. The time step of the time integration was set to 0.25×10^{-7} s to resolve the acoustic pressure propagation through the smallest grids. To simulate the fluid-structure interaction, the forces on each mass $F_{1\alpha}$ and $F_{2\alpha}$ were calculated by integrating the pressure on vocal fold surface, and mass positions and velocities for the next time step were predicted by Eqs. (1) and (2). The Reynolds number based on the inlet flow rate and glottal length was $\text{Re} = U_{in}/l_g\nu = 2352$, similar to that often observed in normal phonation of male vocal folds [e.g., Pelorson *et al.* (1994)].

C. 1D flow model

In the 1D flow simulation, the compressible flow characteristics were modeled by an equivalent circuit. The inertia, flow resistance (e.g., pressure drop and fluid viscosity), and fluid compressibility were modeled as inductance L, resistance R, and capacitance C, respectively. The equivalent circuit for the two-mass model is shown in Fig. 5. For the inlet, the constant pressure of 2 kPa was set as a constant power supply in the same way as the 3D model. Airflow through the pressure chamber, subglottal and supraglottal tracts were modeled as transmission lines of n hard-walled sections, and each element's value was determined by its cross-sectional area A_{n}, circumference S_{n}, and tract length l_{n} in the same way as Ishizaka and Flanagan (1972). The inductances, resistances, and capacitances were calculated as $L_n = \rho l_n/2A_n$, $R_n = \alpha(S_n l_n/A_n^2)\sqrt{\rho\mu\omega/2}$, and $C_n = l_n A_n/\rho c^2$, respectively, where μ is the air viscosity, ω is the natural frequency of the lower mass, and c is the speed of sound. The resistance was set only in the subglottal tract, and the scaling factor of the resistance α was adjusted to $\alpha = 51.85$ to match the subglottal pressure and flow rate in the 3D flow. At the outlet of the vocal tract, the transmission line was terminated by a radiation load of a duct with an infinite baffle L_R and R_R (Flanagan, 1972).

In the flow channel between the two-mass model, the resistance of pressure drop R_k, viscous loss R_v, and glottal inductance L_g were calculated at each time step using the glottal flow rate U_g and areas of the gap between left and right masses for both upper and lower parts (m_1 and m_2). With the inductances and capacitances of the subglottal and supraglottal tracts, a differential equation of the flow rate is written as

$$\begin{aligned}&(R_{k1}+R_{k2})|U_g|U_g + (R_{v1}+R_{v2})U_g \\ &\quad + (L_{g1}+L_{g2}+L_1+L_{sn})\frac{dU_g}{dt} \\ &\quad + \frac{1}{C_1}\int_0^t (U_g - U_1)dt + \frac{1}{C_{sn}}\int_0^t (U_{sn} - U_g)dt = 0. \end{aligned} \tag{7}$$

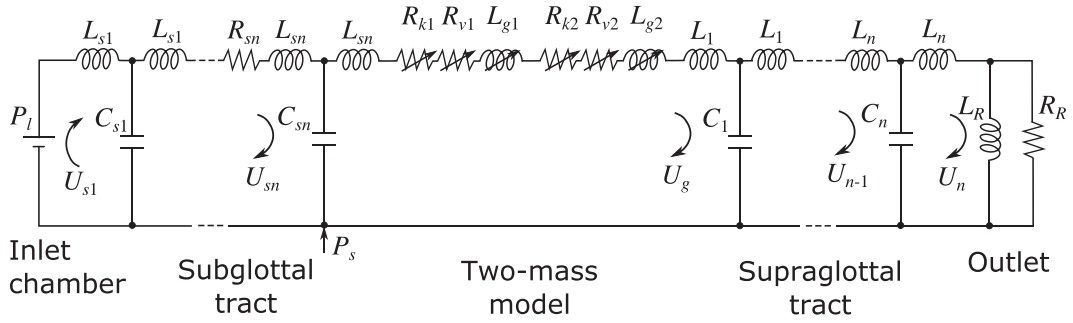

FIG. 5. Equivalent circuit for the one-dimensional flow model.

https://doi.org/10.1121/10.0014949

By solving Eq. (7) using the Newton-Raphson method, the glottal flow rate was calculated at each time step. The time step of the time integration was set to 0.25×10^{-5} s. From the estimated flow rate U_g, the pressure distribution along vocal fold surface and the forces on each mass $F_{1\alpha}$ and $F_{2\alpha}$ were calculated. The surface was divided into 62 points in x_1 direction, and the pressure at each point was calculated as

$$p_{i+1} = p_i + \frac{1}{2}\rho U_g^2\left(\frac{1}{A_i^2} - \frac{1}{A_{i+1}^2}\right) - \frac{12\mu\Delta x_1}{l_g\left((h_i + h_{i+1})/2\right)^3}U_g, \tag{8}$$

where A_i and h_i are the cross-sectional area and the gap width between the left and right fold surfaces at each point. The distance between consecutive points Δx_1 was 0.1 mm. The upstream pressure P_1 was obtained from the pressure at the subglottal tract P_s just upstream from the glottis in the transmission line. In addition, the separation point of the glottal flow was estimated by solving the turbulent boundary layer theory based on Pelorson *et al.* (1994). The pressure downstream from the separation point was assumed to be constant and no pressure recovery was considered. By integrating the pressures on each vocal fold surface, the forces on each mass $F_{1\alpha}$ and $F_{2\alpha}$ were obtained, and mass positions and velocities for the next time step were predicted by Eqs. (1) and (2). These calculations were implemented in the MATLAB (version 2021b, The Mathworks, Inc.), and the code is attached as the supplemental material.[1]

III. RESULTS

A. Comparison of 3D and 1D flows: Pressure distribution and glottal flow

The subglottal pressures P_s of 3D and 1D flow models in the symmetric condition ($Q = 1.0$) are plotted in Fig. 6. The pressure in the 3D flow is sampled at $x_1 = -10.1$ mm in the middle of the subglottal tract. The time was normalized by the period of fundamental frequency f_0. The comparison was generally good, except that acoustic reflections were much stronger in the 3D model. After the complete closure of the two-mass model ($t/T = 0, 1, 2, \ldots$), the subglottal pressure increased up to 4.1 kPa in the 3D model and 3.6 kPa in the 1D model. Then, three ripples appeared within one oscillating cycle. The time between the first and second ripples was 1.92 ms (about 521 Hz) for the 3D model and 1.55 ms (about 645 Hz) for the 1D model, indicating a slightly higher subglottal resonance frequency in the 1D model. This mismatch in subglottal acoustics between the 1D and 3D models also contributed to differences in the intraglottal pressure, as discussed below. The mean subglottal pressure was 1350 Pa in the 3D model and 1300 Pa in the 1D model.

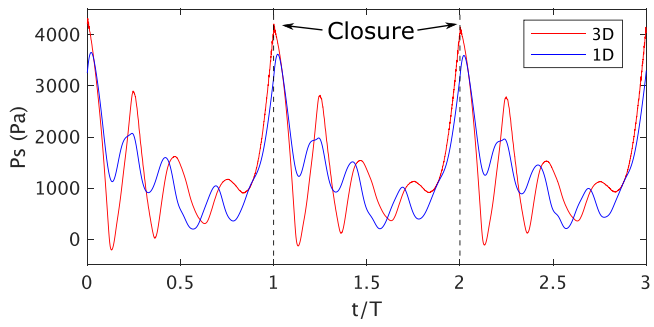

FIG. 6. (Color online) Subglottal pressure P_s of the one-dimensional and the three-dimensional flow models for the symmetric condition ($Q = 1.0$). The pressure in the 3D flow model is sampled at $x_1 = -10.1$ mm.

The flow pressure on the lower and upper masses, glottal flow rate U_g, time derivative of the flow rate dU_g/dt, and its spectrum are plotted for the symmetric ($Q = 1.0$) and asymmetric ($Q = 1.6$) conditions in Fig. 7. The pressures on the left and right folds are plotted with red and black lines, respectively, for the 3D flow model. For the lower masses (top panels in Fig. 7), the flow pressure exhibited similar ripples as the subglottal pressure in both 3D and 1D simulations, as discussed earlier. These ripples also appeared in the pressures on the upper masses (Fig. 7, second row), but only in the open phase of the cycle ($0.23 < t/T < 1.0$) and had much reduced amplitudes. The pressures on the upper masses decreased below -2 kPa when the glottal gap became small ($0.95 < t/T < 1$), at which time the pressures on the lower masses reached the maximum. The differences between the left and right pressures were generally small, even in the asymmetric condition. The maximum difference in the asymmetric condition was 166 Pa (approximately 6%) at $t/T = 1.0$ on the lower masses and 209 Pa (approximately 14%) at $t/T = 0.94$ on the upper masses. These overall tendencies in the 3D flow were reproduced by the 1D model for both symmetric and asymmetric cases. However, the amplitude and phase of ripples were slightly different between the 1D and 3D conditions in the symmetric case (Fig. 7, left panels), due to the similar difference in the subglottal pressure. In particular, the pressure fluctuation in the 3D model at $t/T = 0.2$ was overestimated by the 1D model in the asymmetric case (Fig. 7, right panels), and a sharp trough and peak were observed at $t/T \approx 1$ only in the 1D flow model.

The overall frow rate waveforms in the 3D flow were captured by the 1D model for both symmetric and asymmetric cases (Fig. 7, third row), although the maximum flow rate was underestimated in the 1D flow model by approximately 200 cm^3/s in the symmetric case, and the reverse flow of -250 cm^3/s was not predicted by the 1D flow in the asymmetric case. Fourth row of Fig. 7 shows the time derivative of the flow rate dU_g/dt, often considered as the voice source (Zhang, 2016b). Overall, the dU_g/dt waveforms in the 3D model were captured by the 1D model in both symmetric and asymmetric conditions, except for the slight differences in the amplitudes and phase of the small ripples. The power spectral densities (PSDs) of spectral harmonics for dU_g/dt (Fig. 7, bottom) are compared with a spectral slope of -7 dB/octave. The slopes of the 1D models agreed well with those of the 3D models in both symmetric and asymmetric conditions.

The instantaneous velocity in the glottis and the pressure p on vocal fold surface at selected instants within one oscillation

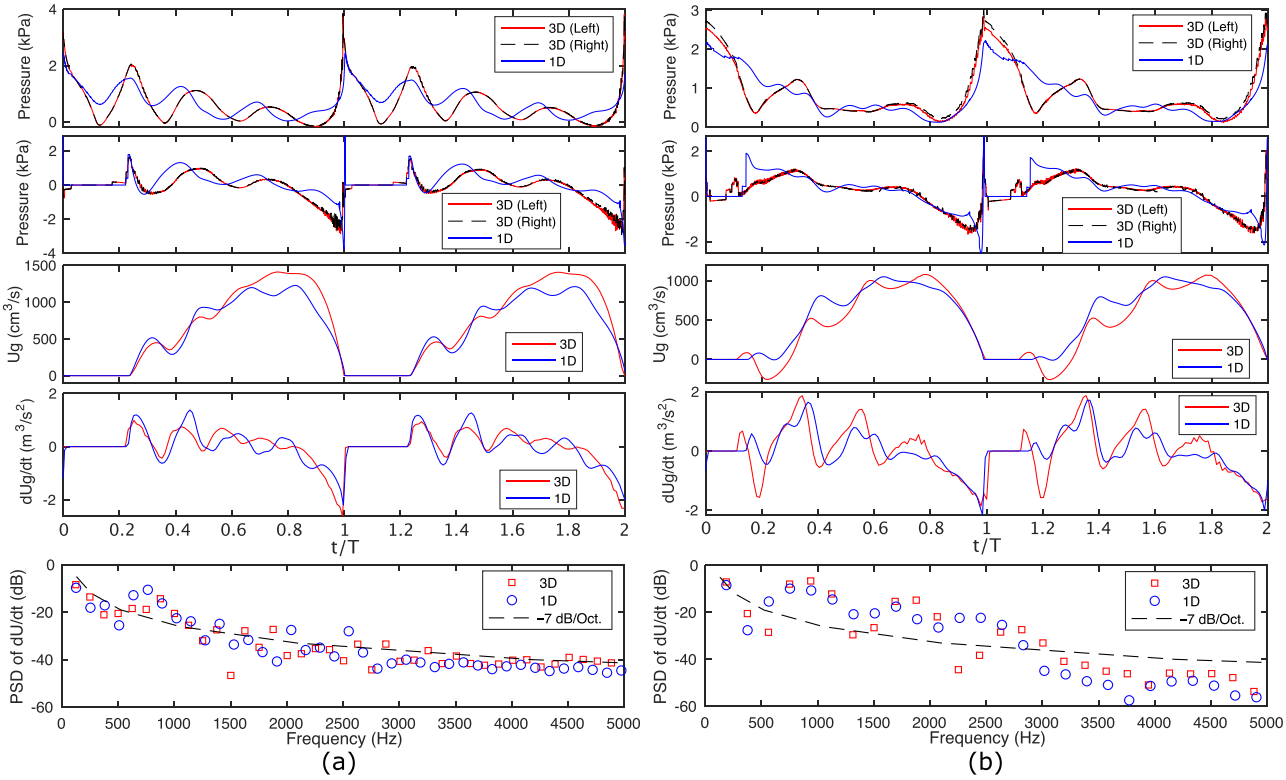

FIG. 7. (Color online) From top to bottom, the pressure on the two lower masses, pressure on the upper masses, the glottal flow rate U_g, time derivative of the glottal flow dU_g/dt as a function of time, and power spectral density (PSD) of harmonics of dU_g/dt, for tension imbalance parameters $Q = 1.0$ (a) and 1.6 (b). For the PSD, the slope of −7 dB/octave is plotted for comparison.

cycle at $t/T = 0.27$ (opening), 0.88 (open), and 0.97 (closing) are shown in Fig. 8 for the symmetric condition ($Q = 1.0$). Movies of the flow velocity and pressure distribution for one cycle are attached as supplemental multimedia.[1] The axis x_1 is normalized by the inferior-superior vocal fold thickness $L = 6.125$ mm. In the 3D flow, pressure fluctuations in the anterior-posterior (x_3) direction were generally small (<150 Pa), and Fig. 8 shows the pressures averaged along the x_3-direction. The pressure predicted from the 1D flow model is labeled as "1D (self-oscillation)" in the figure.

Overall, the agreement between the 1D and 3D models was not good, due to the mismatch in the subglottal and supraglottal pressure, particularly the mismatch in the phases and amplitudes of the small ripples (Fig. 7), as described earlier. To isolate the effect of this difference in the subglottal pressure between the 1D and 3D models and focus on ability of the 1D model to predict intraglottal pressure given the correct subglottal pressure, another 1D estimation of the intraglottal pressure was also calculated using Eq. (8) and the subglottal pressure and vocal fold motion calculated from the 3D model (thus a forced oscillation condition). This pressure is also shown in Fig. 8 and labeled as "1D (forced oscillation)." In general, the agreement between the pressure predicted from the 1D flow under the forced oscillation condition and the pressure predicted from the 3D flow model was much improved, when the same subglottal pressure was used in the two models. Although the two 1D models (self-and forced oscillations) had slightly different vibratory patterns and flow rates, the predicted flow separation points were identical.

At $t/T = 0.27$, the upper masses started opening, and the initial jet flow inclined toward the left side in the 3D flow model. The pressure p decreased from 2.4 to −0.4 kPa along vocal fold surface and the flow separated from the wall at $x_1/L = -0.03$ in the 3D flow, and the pressures on the left and right vocal fold surfaces were almost the same. The pressure predicted from the 1D flow with forced oscillation generally agreed with the pressure in the 3D simulation, whereas the pressure predicted from the 1D flow with self-sustained oscillation underestimated the pressure by 0.8 kPa due to the lower subglottal pressure.

At $t/T = 0.88$, the glottis was fully open. The flow velocity was high, and the flow transitioned to turbulence in the supraglottal tract. Both left and right pressures decreased from 1 kPa, reached the minimum at $x_1/L = -0.32$, and gradually increased toward the glottal outlet. However, there was no reversed flow within the glottis despite an adverse pressure gradient at $x_1/L = -0.3$ and the flow remained attached to vocal fold surface in the 3D flow. In contrast, the flow separation was predicted at $x_1/L = -0.3$ in the 1D flow model. Since we set the pressure downstream from the separation point as constant, the pressure was underestimated by 0.6 kPa with the 1D forced oscillation, whereas the pressure was overpredicted by 0.7 kPa with the 1D self-sustained oscillation at $x_1/L = 0$.

When $t/T = 0.97$, the gap between the left and right masses was 0.28 mm for both upper and lower masses. The glottal flow was further accelerated, and the vocal fold surface pressure reached −3.0 kPa at $x_1/L = -0.3$. While the flow separated at $x_1/L = -0.03$ in the 3D flow, the separation

https://doi.org/10.1121/10.0014949

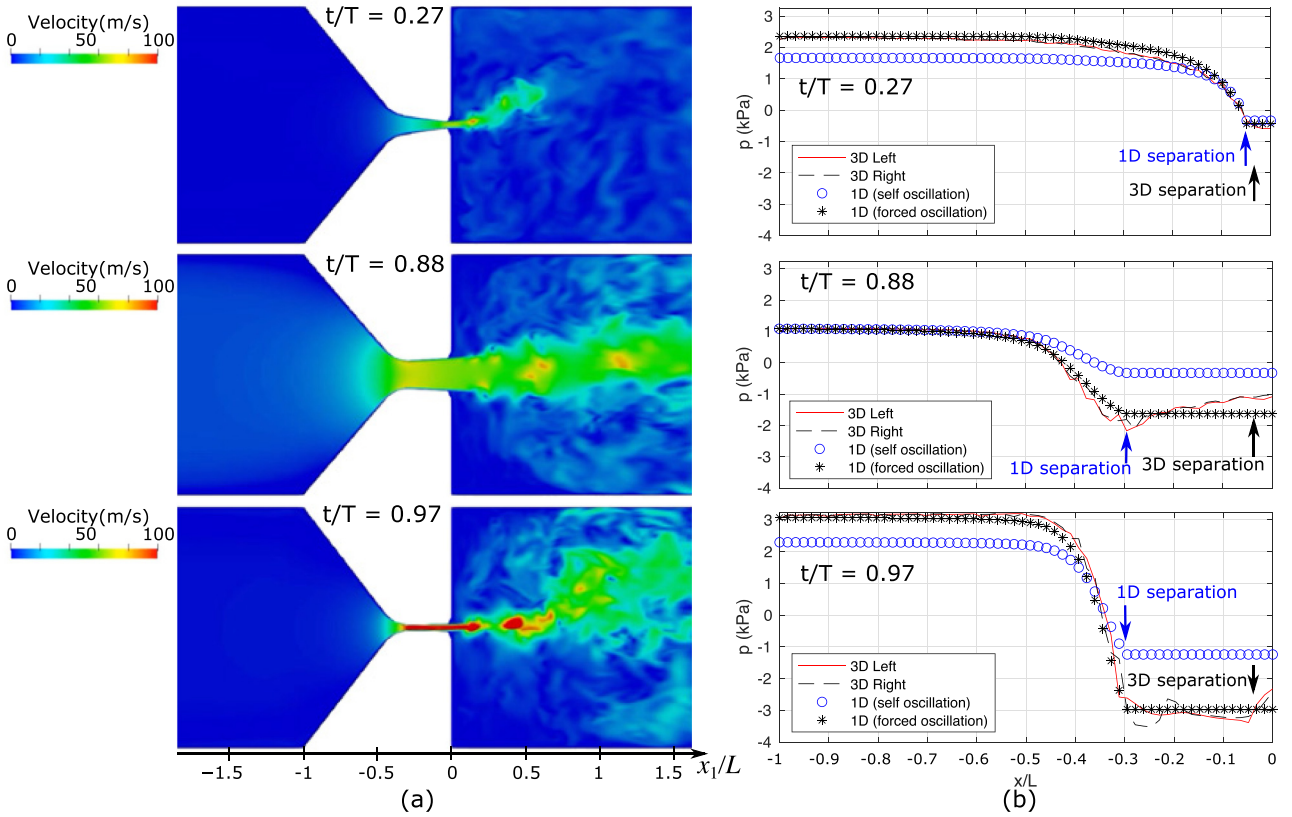

FIG. 8. (Color online) Flow fields and pressure distributions on vocal fold surfaces for the symmetric condition ($Q = 1.0$). The instantaneous velocity magnitudes were shown in (a), while the pressure p and flow separation points are plotted in (b) for normalized time $t/T = 0.27$ (top), $t/T = 0.88$ (center), and $t/T = 0.97$ (bottom). The pressure of the 1D flow was also plotted with the forced oscillation, which uses the displacement and flow rate of the 3D model.

point was estimated at $x_1/L = -0.3$ by the 1D flow. The surface pressure was underestimated by 0.7 kPa at $x_1/L < -0.3$ and overpredicted by 1.7 kPa at $x_1/L > -0.3$ in the 1D self-oscillation condition.

The instantaneous velocity and pressure on vocal fold surface from the 3D simulation at three instants within one oscillation cycle are shown in Fig. 9 for the asymmetric condition ($Q = 1.6$). In the same way as in Fig. 8, two 1D estimations of the pressure on vocal fold surface are shown in Fig. 9: one from the 1D self-sustained oscillation and the other from 1D flow driven by the subglottal pressure predicted from the 3D simulation. In general, the pressure predicted from the 1D forced oscillation agreed well with the pressure from the 3D simulation. The agreement between the 1D self-sustained oscillation and the 3D prediction was poor, but was overall better than that in the symmetric condition in Fig. 8.

When the upper masses started to open at $t/T = 0.16$, the flow was reversed back into the subglottal tract. This can also be observed in the waveform of the flow rate (Fig. 7, right panel). At this instant, the pressure on vocal fold surface increased from 0.4 kPa at the glottal inlet to 0.7 kPa at the outlet on both left and right masses in the 3D flow. This indicates that the reverse flow was caused by the increase in the pressure inside the vocal tract just above the glottis. This increase in the pressure toward the glottal outlet was not predicted by the 1D flow model.

At $t/T = 0.78$, the jet flow exited from the glottal gap and became inclined toward the left side (the top side in Fig. 9) of the vocal tract due to the asymmetric vocal fold motion. Hence, the flow separated from the left wall at $x_1/L = -0.03$, whereas the flow separated from the right wall at $x_1/L = -0.25$. However, the pressures on both the left and right vocal fold surfaces were largely the same. The separation point was predicted at $x_1/L = -0.3$ in both 1D flow models and this agrees with the right side of the 3D flow model. The self-sustained oscillations of the 1D model underestimated the flow pressure for the entire vocal fold surface.

When $t/T = 0.96$, the vocal fold surface on the right (the lower surface in the figure) became convergent whereas the left vocal fold surface was slightly divergent. As a result, the jet flow exiting the glottis was inclined toward the left side in the 3D flow. In contrast, the overall pressure distributions on the left and right surfaces were again almost the same in the 3D flow. The flow separated from the vocal fold surface at $x_1/L = -0.03$ on both sides, and the pressure decreased from approximately 2.5 to −1.7 kPa. The flow separation position and the pressure distributions from both 1D flow models agreed well with those of the 3D flow model.

B. Comparison of overall patterns across a range of tension imbalance

The mass displacements y predicted in the 3D and 1D flow models are shown in Fig. 10 for conditions with the

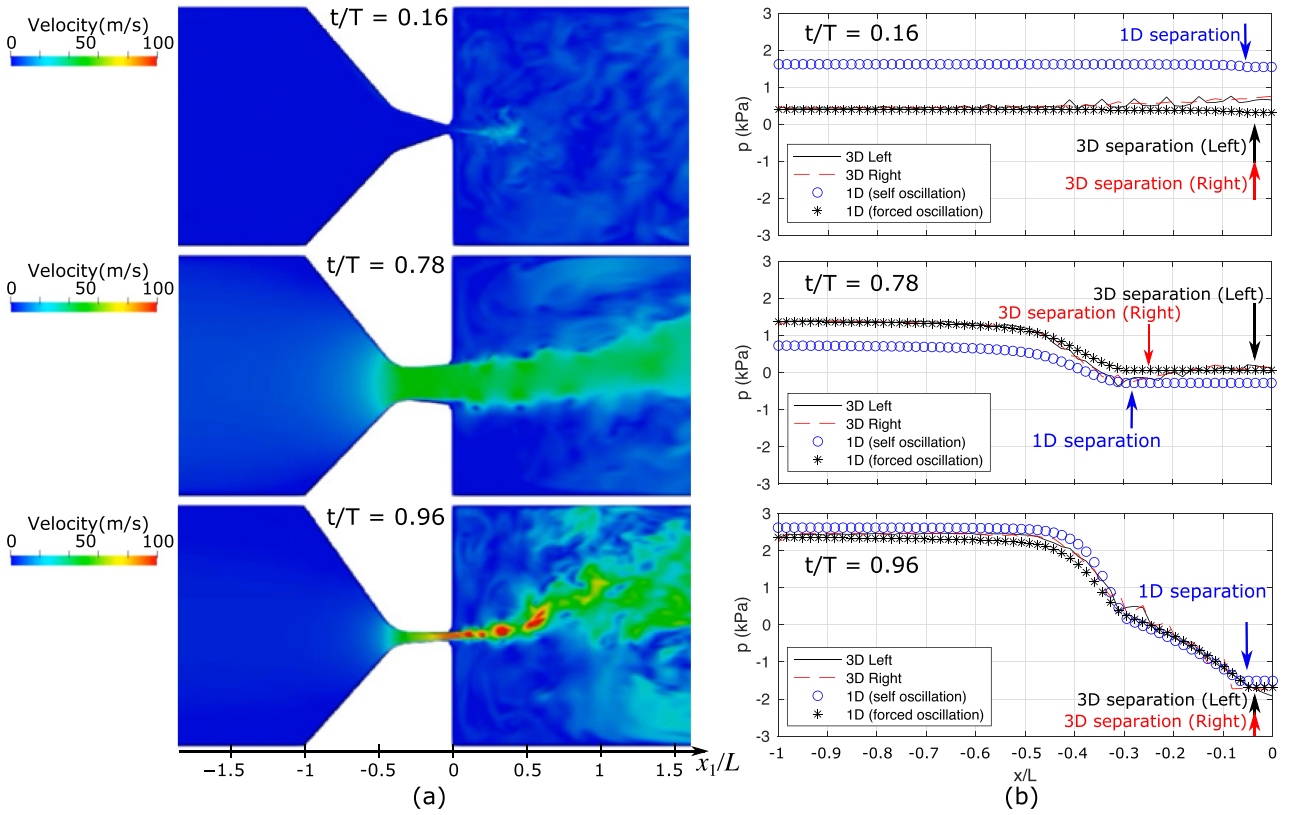

FIG. 9. (Color online) Flow fields and pressure distributions on vocal fold surfaces for the asymmetric condition ($Q = 1.6$). The instantaneous velocity magnitudes are shown in (a), while the pressure drop $p - P_s$ and predicted separation points are plotted in (b) for normalized time $t/T = 0.16$ (top), $t/T = 0.78$ (center), and $t/T = 0.96$ (bottom). The pressure of the 1D flow was also plotted with the forced oscillation, which uses the displacement and flow rate of the 3D model.

tension imbalance parameter $Q = 0.4$, 0.6, 1.0, 1.6, and 3.0. Self-sustained oscillation was achieved for Q values from 0.4 to 1.6 in the 3D flow-based model, and for Q values from 0.6 to 1.6 in the 1D flow-based model. For $Q = 0.6$, 1.0, and 1.6, data were shown after three initial cycles when the oscillation has become stable, and time was normalized by the corresponding period of vocal fold vibration. The general trends of variation in the vibration patterns, including left-right difference in phase and amplitude, were consistent between the 1D and 3D models.

For the left-right symmetric condition ($Q = 1.0$), the left and right masses showed symmetric motion in simulations with both the 3D and 1D flow models. While the left and right vocal fold displacements were exactly the same for the 1D model, a slight difference of less than 2% (< 0.026 mm) was observed between the left and right displacements for the 3D model. The maximum displacement of the upper masses was 1.32 and 1.74 mm for the 3D and 1D models, respectively. The upper masses collided with a penetration depth of approximately 0.25 mm for $1 < t/T < 1.23$, while the lower masses collided briefly at $t/T = 1.05$ for both the 3D and 1D models.

When $Q = 0.4$, the right springs were stiffer than the left springs. The masses oscillated with $f_0 = 53$ Hz in the 3D model and the motion trajectory showed the dicrotic motion. For the 1D flow model, the initial oscillation was similar to that in the 3D model. However, the left and right masses did not collide in the 1D flow, and the oscillation eventually damped out over time. As Q increased to 0.6, the stiffness of the left mass increased and the self-sustained oscillation was achieved in both the 3D and 1D models. Due to the stiffness imbalance, the displacement of the right masses (the stiffer side) was about two times larger than that of the left masses, and one oscillation cycle of the left masses showed double peaks.

When the left springs were stiffer than the right springs with $Q = 1.6$, the displacement amplitudes of the left masses were similar to that of $Q = 1.0$, while the right masses exhibited smaller amplitudes compared to the left masses. The motion of the left mass led in phase by approximately 45°, and only the upper masses collided. For the condition with $Q = 3.0$, the amplitudes of the left masses were significantly reduced, and the displacements of the right masses were larger than those of the left masses initially. However, the left and right masses did not collide, and the oscillation decayed and eventually ceased for both 3D and 1D flow models.

The fundamental frequency f_0, left-right amplitude ratio, phase difference, and the maximum flow declination rate (MFDR) are compared in Fig. 11. The fundamental frequency f_0 increased as the tension imbalance parameter Q increased from 0.4 to 0.8 and from 1 to 1.6 for the 3D flow model. This tendency was reproduced by the 1D flow model, except for $Q = 0.4$ for which the vibration in the 1D model exhibited a similar f_0 but eventually damped out.

https://doi.org/10.1121/10.0014949

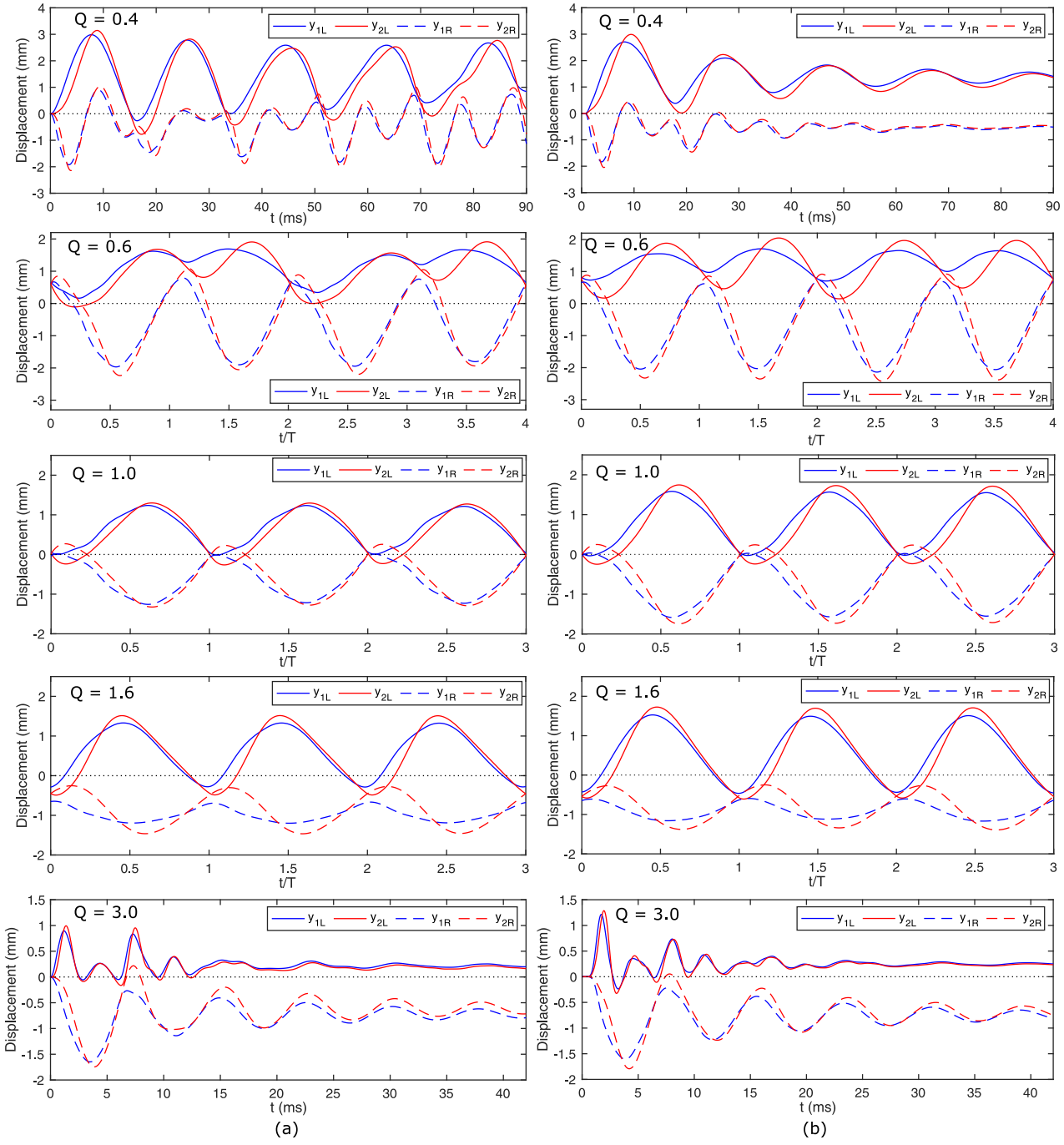

FIG. 10. (Color online) Displacement of each mass for the 3D (a) and 1D (b) flow models. The tension imbalance parameter was changed from $Q = 0.4$ to 0.6, 1.0, 1.6, and 3.0. The solid lines show left mass trajectories, whereas the dashed lines show right mass trajectories.

The left-right amplitude ratio and phase difference also increased in the range from $Q = 0.6$ to 1.6 of the 3D flow model, and these values were predicted by the 1D flow model from $Q = 0.8$ to 1.2. The 1D flow model overestimated the left-right amplitude ratio for $Q = 1.4$ and 1.6 and underestimated the phase difference for $Q = 0.6$.

The MFDR was calculated as the negative peak value of the time derivative of flow rate dU_g/dt. Since dU_g/dt represents the sound source waveform, the minimum of dU_g/dt determines the peak amplitude of the produced voice, i.e., the voice intensity (Zhang, 2016b). The maximum of MFDR appeared when $Q = 0.6$, and in general the effect of Q on the MFDR is small in the range investigated. The values simulated with the 1D flow model were generally in good agreement with these values, except for $Q = 0.6$, where it was 21% underestimated.

The overall trends in Fig. 11 are consistent with the experimental observation in Zhang and Luu (2012). They showed the existence of two regimes of distinct vibratory pattern, one for conditions with small left-right stiffness asymmetry and the other for conditions of large left-right stiffness asymmetry. In Fig. 11, conditions with Q values

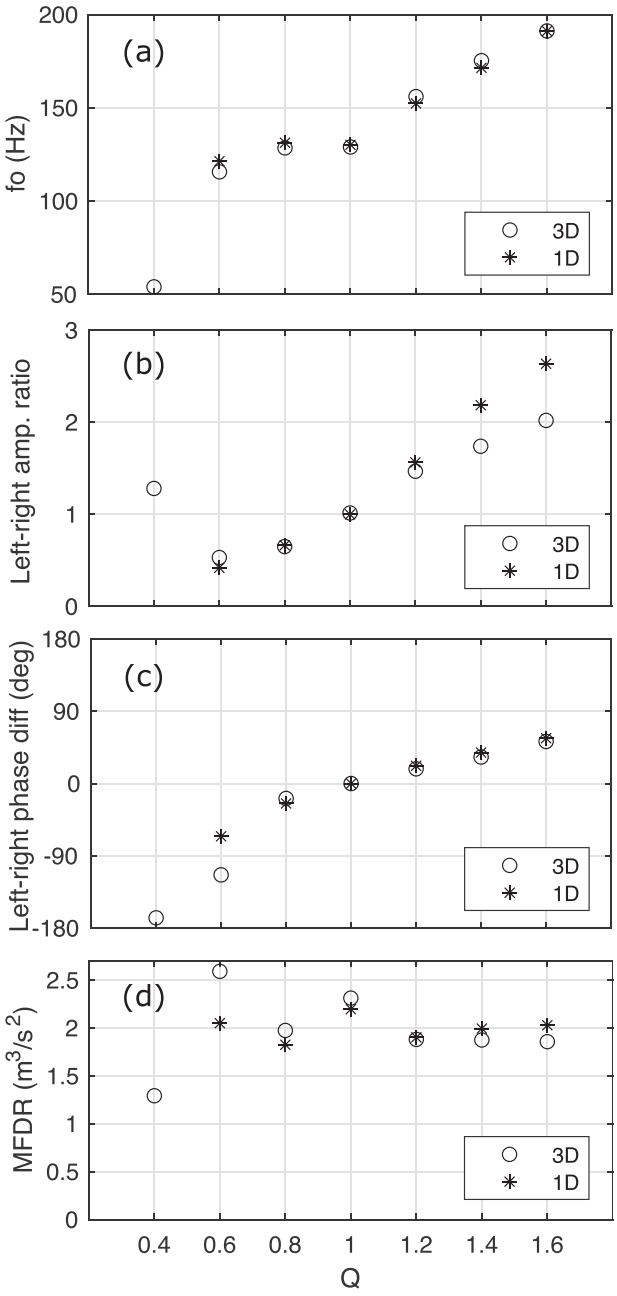

FIG. 11. Dependence of oscillation characteristics on the tension imbalance parameter Q. The fundamental frequency f_0 (a), left-right amplitude ratio (b), phase difference (c), and the maximum flow declination rate (MFDR) (d) are plotted from $Q = 0.4$ to 1.6.

been 0.6 and 1.6 appear to belong to the regime of small left-right stiffness asymmetry, with the vocal folds exhibiting comparable vibration amplitude and the stiffer side leading in phase. The conditions with $Q = 0.4$ and 3.0 correspond to the transition to the regime of large left-right stiffness asymmetry, with the vibration dominated by the softer vocal fold.

IV. DISCUSSION

The results of this study showed that the vocal fold vibration pattern and voice outcome measures can be predicted by the 1D flow model with reasonable accuracy not only for the symmetric but also for the asymmetric conditions. Although the maximum vocal fold displacement was slightly overestimated by the 1D model for all cases, the general trends of variation in the vibration pattern, f_0, left-right amplitudes ratio, and phase difference with increasing Q in the 1D model agreed well with those in the 3D flow model. The results also indicate that the intraglottal pressure can be simulated with the quasi-steady approximation in Eq. (8) and this observation agrees with previous experimental studies (Zhang *et al.*, 2002; Ruty *et al.*, 2007; Farahani and Zhang, 2016; Honda *et al.*, 2022).

It is worth noting that this agreement was obtained despite the differences in the flow pressure on vocal fold surface predicted by the 1D and 3D flow models, particularly in the symmetric case (Fig. 8). This suggests that while the vocal folds cannot vibrate without the glottal flow, vocal fold structural properties have a larger role than the glottal flow in determining the overall vibratory pattern and voice production, as shown in our earlier studies (Farahani and Zhang, 2014; Zhang, 2016b).

The slight overestimation of the displacement in the 1D model may be caused by the difference in the subglottal pressure predicted by the 1D and 3D flow models (Fig. 6). Further improvement of the 1D model thus can be achieved by more accurately modeling subglottal and supraglottal acoustics and their effects on the intraglottal pressure. Indeed, by using the subglottal pressure of the 3D flow in the 1D model (forced oscillation in Figs. 8 and 9), the flow pressure on vocal fold surface was more accurately predicted, except for the reverse flow in the asymmetric condition.

In this study, both the subglottal and intraglottal pressures exhibited ripples that were associated with acoustic reflections from both the subglottal and supraglottal tracts. These ripples also appeared in the waveforms of flow rate and voice source dU_g/dt, suggesting some impact of source-tract interaction on the voice source. However, these ripples (about 600 Hz) did not appear in the waveforms of vocal fold motion. This indicates a small influence of subglottal and supraglottal acoustics on the vibration patterns when the fundamental frequency is not sufficiently close to sub- or supra-glottal acoustic resonances, as shown in previous experiments (Zhang, *et al.*, 2006). In other words, source-tract interaction impacted mainly the glottal flow but not vocal fold vibration in our study.

The relatively small difference between 1D and 3D flow models is consistent with the results from Decker and Thomson (2007) which compared 1D and 2D flows in left-right symmetric conditions. In contrast, de Vries *et al.* (2002) reported relatively large differences in oscillation characteristics between the 2D and 1D flow models. These large differences may be related to the relatively coarse mesh used in their study. As described in the Appendix, the mass trajectories and oscillation frequency may vary significantly depending on the grid size. The relatively large grid sizes in de Vries *et al.* (2002) might have caused the large differences between their 1D and 2D simulations.

https://doi.org/10.1121/10.0014949

Tao *et al.* (2007) reported asymmetric vocal fold vibration in left-right symmetric vocal fold conditions. This is different from the observation in our study that the vibration pattern was symmetric under the left-right symmetric condition with $Q = 1$. This contradiction was probably caused by the difference in the simulation conditions such as the size of the masses. Since the upper and lower mass sizes were the same and the coupling spring constant was smaller in Tao *et al.* (2007), the left-right difference in the intraglottal pressure might be sufficient to induce asymmetric vocal fold vibration. Note that this phenomenon (asymmetric vibration induced by asymmetric intraglottal pressure) is ruled out in the 1D flow model by its design.

V. CONCLUSION

In this study, we compared voice production predicted by 1D and 3D flow simulations coupled to a two-mass model at left-right symmetric and asymmetric vocal fold conditions. The results showed that the vocal fold vibration pattern, including left-right difference in vibration amplitude and phase, and the voice outcome measures can be predicted by the 1D flow model with reasonable accuracy for both symmetric and asymmetric conditions. When the vocal folds exhibited left-right asymmetric vibration, the differences in the flow pressure on the left and right vocal fold surfaces were generally small, even if the glottal flow was inclined and separated from the wall at different locations on the left and right vocal fold surfaces. The agreement in the overall vocal fold vibration pattern was obtained despite some discrepancies in the predicted vocal fold surface pressures between the 1D and 3D flow models, suggesting that vocal fold properties have a larger role than the glottal flow in determining the overall vibratory pattern. The agreement may be further improved by more accurately predicting the subglottal and supraglottal pressures. Future work will focus on validating the 1D flow model in vocal fold models with more realistic vocal fold movement (Adachi and Yu, 2005) and geometry (Wu and Zhang, 2021), and for laryngeal sizes typical of female and children.

ACKNOWLEDGMENTS

This work was supported by MEXT as JSPS KAKENHI, Grant-in-Aid for Young Scientists (Grant No. JP20K14648) and research Grant No. R01DC001797 from the National Institute on Deafness and Other Communication Disorders, the National Institutes of Health. We acknowledge Dr. Hiroshi Yokoyama for his contributions to the development of the 3D flow simulation codes.

APPENDIX: COMPUTATIONAL ACCURACY OF THE 3D FLOW MODEL

To evaluate the computational accuracy of the 3D flow simulation, we investigated the convergence of the grid resolutions and compared the pressure distributions with experimental measurements. The list of grid sizes used is shown in Table II. We constructed five computational grids with gradually reduced minimum mesh size, as shown in Table II. The time step was also reduced depending on the minimum grid size to keep the same CFL number based on the speed of sound. The total number of grids was increased from 12.5×10^6 of Mesh1 to 74.0×10^6 of Mesh5. The fundamental frequency f_0 and open quotient (OQ) of mass trajectories were calculated after obtaining the stable self-sustained oscillation (Fig. 12). The f_0 decreased from 143 Hz of Mesh1 to 127 Hz of Mesh4, and f_0 of Mesh 4 was almost the same with that of Mesh5. The OQ also decreased from 0.873 of Mesh1 to 0.762 of Mesh4, and OQ slightly increased to 0.765 in Mesh 5. These results indicate that the motion trajectories of Mesh4 and Mesh5 were almost the same and the result converged with the grid resolution of Mesh4.

TABLE II. The minimum grid size, corresponding time step of time integration, and total number of grids of each computational grid sets.

	Δx_1 (mm)	Δx_2 (mm)	Δx_3 (mm)	Δt (s)	No. Grids
Mesh1	0.1	0.1	0.2	1.0×10^{-7}	12.5×10^6
Mesh2	0.05	0.05	0.1	5.0×10^{-8}	42.3×10^6
Mesh3	0.05	0.033	0.1	2.5×10^{-8}	52.9×10^6
Mesh4	0.05	0.025	0.1	2.5×10^{-8}	63.4×10^6
Mesh5	0.05	0.02	0.1	2.5×10^{-8}	74.0×10^6

Then, we compared the pressure distributions of Mesh4 to the intraglottal pressure distribution experimentally measured in static vocal fold replicas as reported in Scherer *et al.* (2001). The symmetric and asymmetric vocal fold geometries in Scherer *et al.* (2001) were simulated in this study. The subglottal pressure was kept at 1.5 kPa in both the experiment and simulation. The simulated pressure distributions are plotted in Fig. 13. For both symmetric and asymmetric geometry, the overall pressure distribution of the simulation agreed well with the measurement. The difference in the pressure distributions between the flow-attached wall and the other side was reproduced by the simulation. However, slight differences between the experiment and simulation appeared near the glottal entrance, indicating that the rounded constriction is still difficult to represent in the immersed boundary method with the current grid resolution. Nevertheless, we confirmed that our 3D computational

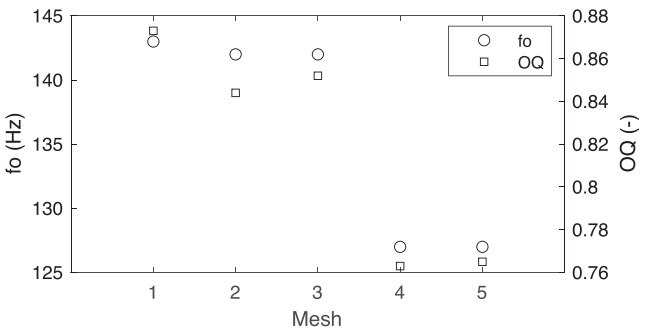

FIG. 12. Fundamental frequency f_0 and open quotient (OQ) of the mass trajectories calculated with the 3D flow simulation with five grid resolutions.

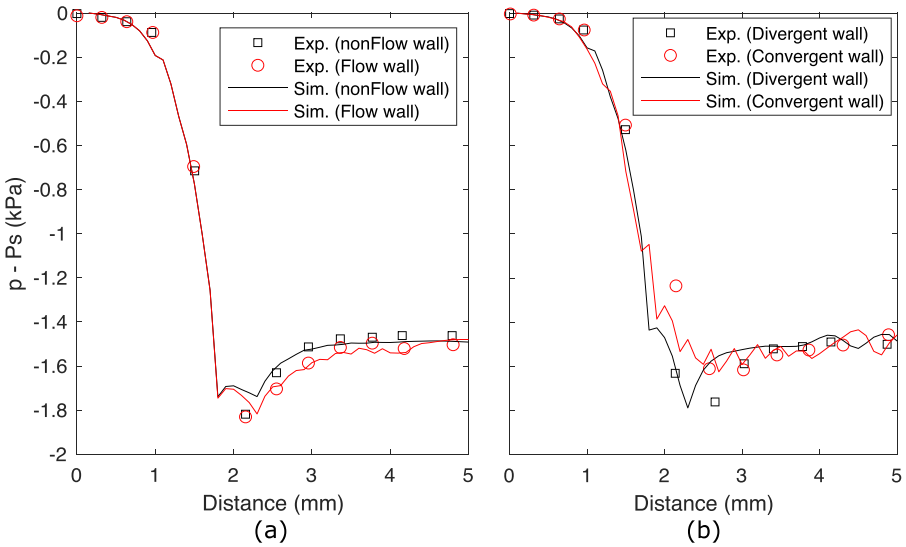

FIG. 13. (Color online) Pressure distribution on the surfaces of static vocal fold geometries. The experimental values were from the experiment by Scherer *et al.* (2001). The pressures on flow attached walls and the other side are separately plotted in both symmetric (a) and asymmetric (b) geometries.

model using Mesh4 can reproduce the pressure distribution in the static vocal fold models with reasonable accuracy and decided to use Mesh4 in this study.

[1]See supplementary material at https://www.scitation.org/doi/suppl/10.1121/10.0014949 for the MATLAB code of the 1D flow model (SuppPub1.m) and a movie of velocity and pressure distributions for the symmetric ($=1.0$) and asymmetric ($=1.6$) conditions (SuppPubmm1.mp4 and SuppPubmm2.mp4).

Adachi, S., and Yu, J. (**2005**). "Two-dimensional model of vocal fold vibration for sound synthesis of voice and soprano singing," J. Acoust. Soc. Am. **117**(5), 3213–3224.

Birkholz, P., Martin, L., Willmes, K., Kröger, B. J., and Neuschaefer-Rube, C. (**2015**). "The contribution of phonation type to the perception of vocal emotions in German: An articulatory synthesis study," J. Acoust. Soc. Am. **137**(3), 1503–1512.

Decker, G. Z., and Thomson, S. L. (**2007**). "Computational simulations of vocal fold vibration: Bernoulli versus Navier–Stokes," J. Voice **21**(3), 273–284.

de Vries, M. P., Schutte, H. K., Veldman, A. E. P., and Verkerke, G. J. (**2002**). "Glottal flow through a two-mass model: Comparison of Navier–Stokes solutions with simplified models," J. Acoust. Soc. Am. **111**(4), 1847–1853.

Elie, B., and Laprie, Y. (**2016**). "Extension of the single-matrix formulation of the vocal tract: Consideration of bilateral channels and connection of self-oscillating models of the vocal folds with a glottal chink," Speech Commun. **82**, 85–96.

Falk, S., Kniesburges, S., Schoder, S., Jakubaß, B., Maurerlehner, P., Echternach, M., Kaltenbacher, M., and Döllinger, M. (**2021**). "3D-FV-FE aeroacoustic larynx model for investigation of functional based voice disorders," Front. Physiol. **12**, 616985.

Farahani, M. H., and Zhang, Z. (**2014**). "A computational study of the effect of intraglottal vortex-induced negative pressure on vocal fold vibration," J. Acoust. Soc. Am. **136**(5), EL369–EL375.

Farahani, M. H., and Zhang, Z. (**2016**). "Experimental validation of a three-dimensional reduced-order continuum model of phonation," J. Acoust. Soc. Am. **140**(2), EL172–EL177.

Flanagan, J. L. (**1972**). *Speech Analysis Synthesis and Perception* (Springer-Verlag, Berlin).

Honda, T., Kanaya, M., Tokuda, I. T., Bouvet, A., Van Hirtum, A., and Pelorson, X. (**2022**). "Experimental study on the quasi-steady approximation of glottal flows," J. Acoust. Soc. Am. **151**(5), 3129–3139.

Ishizaka, K., and Flanagan, J. L. (**1972**). "Synthesis of voiced sounds from a two-mass model of the vocal cords," Bell Syst. Tech. J. **51**(6), 1233–1268.

Ishizaka, K., and Isshiki, N. (**1976**). "Computer simulation of pathological vocal-cord vibration," J. Acoust. Soc. Am. **60**(5), 1193–1198.

Kaburagi, T., and Tanabe, Y. (**2009**). "Low-dimensional models of the glottal flow incorporating viscous-inviscid interaction," J. Acoust. Soc. Am. **125**(1), 391–404.

Liu, Q., and Vasilyev, O. V. (**2007**). "A Brinkman penalization method for compressible flows in complex geometries," J. Comput. Phys. **227**(2), 946–966.

Maeda, S. (**1982**). "A digital simulation method of the vocal-tract system," Speech Commun. **1**, 199–229.

McGowan, R. S., Koenig, L. L., and Löfqvist, A. (**1995**). "Vocal tract aerodynamics in /aCa/ utterances: Simulations," Speech Commun. **16**(1), 67–88.

Mergell, P., Herzel, H., and Titze, I. R. (**2000**). "Irregular vocal-fold vibration—High-speed observation and modeling," J. Acoust. Soc. Am. **108**(6), 2996–3002.

Migimatsu, K., and Tokuda, I. T. (**2019**). "Experimental study on nonlinear source–filter interaction using synthetic vocal fold models," J. Acoust. Soc. Am. **146**(2), 983–997.

Neubauer, J., Zhang, Z., Miraghaie, R., and Berry, D. A. (**2007**). "Coherent structures of the near field flow in a self-oscillating physical model of the vocal folds," J. Acoust. Soc. Am. **121**(2), 1102–1118.

Pelorson, X., Hirschberg, A., Van Hassel, R. R., Wijnands, A. P. J., and Auregan, Y. (**1994**). "Theoretical and experimental study of quasisteady flow separation within the glottis during phonation. Application to a modified two-mass model," J. Acoust. Soc. Am. **96**(6), 3416–3431.

Pickup, B. A., and Thomson, S. L. (**2009**). "Influence of asymmetric stiffness on the structural and aerodynamic response of synthetic vocal fold models," J. Biomech. **42**(14), 2219–2225.

Ruty, N., Pelorson, X., Van Hirtum, A., Lopez-Arteaga, I., and Hirschberg, A. (**2007**). "An *in vitro* setup to test the relevance and the accuracy of low-order vocal folds models," J. Acoust. Soc. Am. **121**(1), 479–490.

Scherer, R. C., Shinwari, D., De Witt, K. J., Zhang, C., Kucinschi, B. R., and Afjeh, A. A. (**2001**). "Intraglottal pressure profiles for a symmetric and oblique glottis with a divergence angle of 10 degrees," J. Acoust. Soc. Am. **109**(4), 1616–1630.

Steinecke, I., and Herzel, H. (**1995**). "Bifurcations in an asymmetric vocal-fold model," J. Acoust. Soc. Am. **97**(3), 1874–1884.

Story, B. H., and Titze, I. R. (**1995**). "Voice simulation with a body-cover model of the vocal folds," J. Acoust. Soc. Am. **97**(2), 1249–1260.

Tao, C., Zhang, Y., Hottinger, D. G., and Jiang, J. J. (**2007**). "Asymmetric airflow and vibration induced by the Coanda effect in a symmetric model of the vocal folds," J. Acoust. Soc. Am. **122**(4), 2270–2278.

Titze, I. R., and Talkin, D. T. (**1979**). "A theoretical study of the effects of various laryngeal configurations on the acoustics of phonation," J. Acoust. Soc. Am. **66**(1), 60–74.

Wu, L., and Zhang, Z. (**2021**). "Impact of the paraglottic space on voice production in an MRI-based vocal fold model," J. Voice (published online).

Xue, Q., Mittal, R., Zheng, X., and Bielamowicz, S. (**2010**). "A computational study of the effect of vocal-fold asymmetry on phonation," J. Acoust. Soc. Am. **128**(2), 818–827.

https://doi.org/10.1121/10.0014949

Yoshinaga, T., Nozaki, K., and Iida, A. (**2020**). "Hysteresis of aeroacoustic sound generation in the articulation of [s]," Phys. Fluids **32**(10), 105114.
Yoshinaga, T., Arai, T., Inaam, R., Yokoyama, H., and Iida, A. (**2021**). "A fully coupled fluid-structure-acoustic interaction simulation on reed-type artificial vocal fold," Appl. Acoust. **184**, 108339.
Zañartu, M., Mongeau, L., and Wodicka, G. R. (**2007**). "Influence of acoustic loading on an effective single mass model of the vocal folds," J. Acoust. Soc. Am. **121**(2), 1119–1129.
Zhang, Z. (**2016a**). "Cause-effect relationship between vocal fold physiology and voice production in a three-dimensional phonation model," J. Acoust. Soc. Am. **139**(4), 1493–1507.
Zhang, Z. (**2016b**). "Mechanics of human voice production and control," J. Acoust. Soc. Am. **140**(4), 2614–2635.
Zhang, Z. (**2017**). "Toward real-time physically-based voice simulation: An eigenmode-based approach," Proc. Mtgs. Acoust. **30**, 060002.
Zhang, Z., and Luu, T. H. (**2012**). "Asymmetric vibration in a two-layer vocal fold model with left-right stiffness asymmetry: Experiment and simulation," J. Acoust. Soc. Am. **132**(3), 1626–1635.
Zhang, Z., Mongeau, L., and Frankel, S. (**2002**). "Experimental verification of the quasi-steady approximation for aerodynamic sound generation by pulsating jets in tubes," J. Acoust. Soc. Am. **112**(4), 1652–1663.
Zhang, Z., Neubauer, J., and Berry, D. A. (**2006**). "The influence of subglottal acoustics on laboratory models of phonation," J. Acoust. Soc. Am. **120**(3), 1558–1569.